ACS Energy LETTERS

http://pubs.acs.org/journal/aelccp

LETTER

Doped Halide Perovskite Nanocrystals for Reabsorption-Free Luminescent Solar Concentrators

Francesco Meinardi,[*,†,‡] Quinten A. Akkerman,[§,∥] Francesco Bruni,[‡] Sungwook Park,[∥,⊥] Michele Mauri,[†,‡] Zhiya Dang,[§] Liberato Manna,[*,∥] and Sergio Brovelli[*,†,‡]

[†]Dipartimento di Scienza dei Materiali, Università degli Studi di Milano Bicocca, via R. Cozzi 55, I-20125 Milano, Italy

[‡]Glass to Power Srl, Francesco Daverio, 6, I-20135 Milano, Italy

[§]Dipartimento di Chimica e Chimica Industriale, Università degli Studi di Genova, via Dodecaneso 31, I-16146 Genova, Italy

[∥]Istituto Italiano di Tecnologia, via Morego 30, I-16163 Genova, Italy

[⊥]Department of Physics, Pukyong National University, Busan 608-737, Korea

S *Supporting Information*

ABSTRACT: **Halide perovskite nanocrystals (NCs) are promising solution-processed emitters for low-cost optoelectronics and photonics. Doping adds a degree of freedom for their design and enables us to fully decouple their absorption and emission functions. This is paramount for luminescent solar concentrators (LSCs) that enable fabrication of electrode-less solar windows for building-integrated photovoltaic applications. Here, we demonstrate the suitability of manganese-doped $CsPbCl_3$ NCs as reabsorption-free emitters for large-area LSCs. Light propagation measurements and Monte Carlo simulations indicate that the dopant emission is unaffected by reabsorption. Nanocomposite LSCs were fabricated via mass copolymerization of acrylate monomers, ensuring thermal and mechanical stability and optimal compatibility of the NCs, with fully preserved emission efficiency. As a result, perovskite LSCs behave closely to ideal devices, in which all portions of the illuminated area contribute equally to the total optical power. These results demonstrate the potential of doped perovskite NCs for LSCs, as well as for other photonic technologies relying on low-attenuation long-range optical wave guiding.**

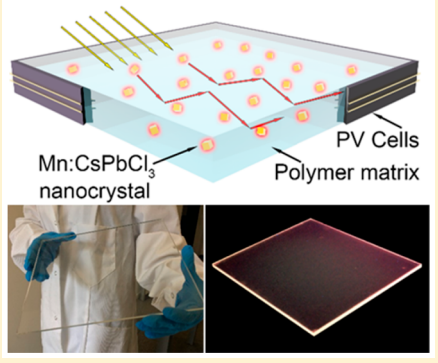

Lead halide perovskite nanocrystals (NCs), in both their hybrid organic−inorganic $MAPbX_3$ (MA = $[CH_3NH_3]^+$, X = Cl, Br, I) composition[1−3] and the fully inorganic cesium lead halide $CsPbX_3$ form,[4−6] have recently emerged as potential candidates in a variety of optoelectronic and photonic technologies,[7] spanning from photovoltaic cells[8,9] and photodetectors[10,11] to light-emitting diodes[12−18] and lasers.[19−21] Similar to other semiconductor NCs, the optical properties of perovskite NCs are tunable through control of the particle size,[1,6,22] shape,[2,6,23,24] and composition that can be easily varied through postsynthesis halide exchange reactions,[4,6] enabling one to obtain narrow emission spectra covering the whole visible spectrum. Spectral tunability by halide exchange has also been shown in hybrid organic/inorganic perovskites. Because of such an applicative potential, numerous studies have recently been dedicated to fundamental and applied chemical and physical investigations of perovskite NCs, including advanced synthesis and material processing routes[25−30] and spectroscopic studies of intrinsic and extrinsic excitonic processes at the ensemble[31,32] and single-particle levels[33−37] also in controlled temperature,[35,38] magnetic field,[32] pressure,[39] chemical,[40] and environmental conditions.[41]

Doping of perovskite NCs has also been recently demonstrated using a variety of transition metal atoms including manganese,[42−45] cadmium, zinc, and tin,[46] leading, in the case of Mn (and bismuth in bulk crystals[47]), to widely Stokes shifted luminescence arising from radiative electronic transitions between intragap states of the dopant impurities sensitized by the NC host. This dopant-mediated emission mechanism is particularly important for perovskite NCs, because established wave function engineering approaches based on heterostructuring, which are commonly adopted to control the excitonic processes and the emission Stokes shift in chalcogenide NCs,[48−51] are difficult to realize in this material system due to the characteristic high ionic mobility leading to rapid alloying of the whole NC structure. By enabling us to

Received: August 4, 2017
Accepted: September 11, 2017
Published: September 15, 2017

DOI: 10.1021/acsenergylett.7b00701
ACS Energy Lett. 2017, 2, 2368−2377

decouple the optical absorption by the NC host from the emission function of the guest impurity, doping might markedly extend the applicative potential of perovskite NCs, potentially paving the way to their use in emerging photon management technologies, in which a wide spectral separation between the absorption and emission bands is key for efficient device performances. One recent example of the potential of this approach has been demonstrated by Wang et al., who used Mn/$CsPbCl_3$ NCs as downconverters for enhancing both the efficiency and the stability of perovskite solar cells.[52]

One of the most compelling classes of photonic devices relying on so-called Stokes shift engineered emitters are luminescent solar concentrators (LSCs),[53,54] which have recently been proposed as an effective complement to conventional photovoltaic modules for the realization of building-integrated photovoltaic (BIPV) devices, such as semitransparent PV windows potentially capable of converting the facades of urban buildings into distributed energy generation units.[55−58] A typical LSC consists of a plastic or glass optical waveguide doped or coated with emissive materials (Figure 1a).[54,59] Direct as well as diffused sunlight penetrates the matrix and is absorbed by the emitters that reradiate it as longer-wavelength fluorescence. Total internal reflection ensures propagation of the emitted light to the waveguide edges, where small PV cells installed along the slab perimeter convert it into electricity (Figure 1a).[55,58,60,61] With respect to other BIPV devices, LSCs offer a series of advantages due to both their all-optical functioning mechanism and their design/fabrication versatility: (i) By collecting sunlight over a large area, the LSC design greatly increases the flux of radiation incident onto the perimeter PV devices, thus enhancing the photocurrent;[54,55] (ii) because LSCs use small amounts of PV material for the photon-to-electron conversion, they allow the use of PV devices with higher efficiency than conventional Si cells that would be prohibitively expensive to adopt in large quantities; (iii) indirect illumination of the perimeter cells by the waveguide makes LSCs nearly unaffected by efficiency losses and electrical stresses due to shadowing effects that occur in bulk and thin-film PVs; and (iv) LSCs can be produced with unmatched freedom in terms of shape, transparency, color, and flexibility, and their design enables the collection of solar energy using electrode-less semitransparent waveguides with essentially no aesthetic impact,[57,62−64] which are ideally suitable for BIPV glazing systems and might provide architects a tool to further enhance the aesthetical value of a building.[65,66] Despite such promise, the widespread use of LSCs has long been hindered by the lack of emitters with sufficiently small spectral overlap between their absorption and emission profiles to suppress reabsorption of the guided luminescence,[67−69] which leads to severe optical losses in large-area devices. This is due to both enhanced nonradiative decay probability scaling exponentially with the number of reradiation events and the isotropic nature of the emission process, which randomizes the propagation direction of guided light, increasing the portion of emitted photons approaching the LSC surface within the escape cone for total internal reflection dictated by Snell's law. In general, for conventional poly(acrylate) waveguides with refractive index $n \approx 1.5$, the maximum light trapping efficiency $\eta_{TR} = \sqrt{(1 - 1/n^2)} = 75\%$, resulting in 25% optical loss at any reabsorption/re-emission event.[55,67] In nontransparent LSCs, escape cone losses can be reduced by using photonic mirrors[70,71] or back-reflectors[63,72,73] that help recycle escaped photons back in the waveguide, thereby enhancing the device efficiency.

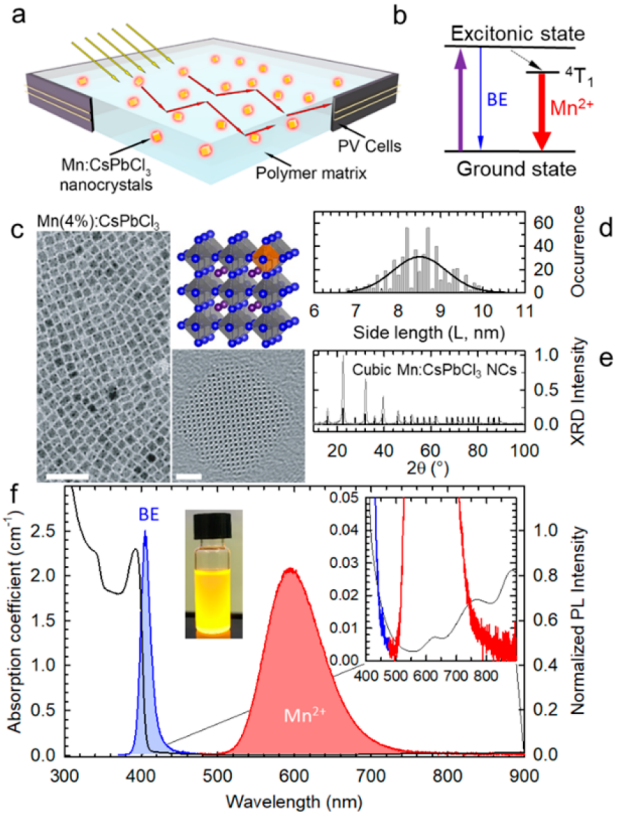

Figure 1. NC-LSC concept and structural and optical properties of Mn-doped $CsPbCl_3$ NCs. (a) Schematic representation of a LSC made of a polymer matrix comprising Mn/$CsPbCl_3$ NCs. (b) Schematic representation of a three-level manganese-doped $CsPbCl_3$ NC. The band edge (BE) and Mn^{2+} photoluminescence (PL) following UV excitation (purple arrow) are shown by blue and red arrows, respectively. Structural data of 4% Mn-doped $CsPbCl_3$ NCs with (c) a transmission electron micrograph (TEM; the scale bar corresponds to 50 and 2 nm in the inset) and (d) related size histogram extracted from analysis of 400 particles, showing cubic NCs with an average side length of 8.6 ± 0.6 nm. (e) XRD pattern of Mn/$CsPbCl_3$ perovskite NCs at room temperature (red line) compared to the XRD patterns of bulk cubic $CsPbCl_3$ perovskite (reference pattern 98-020-1251). (f) Optical absorption (black line) and PL spectra of Mn/$CsPbCl_3$ NCs (4% doping level) under 390 nm excitation in toluene solution. The BE and Mn-related PL bands are highlighted by blue and red shading, respectively. A photograph of the solution under 365 nm excitation highlights the dominant yellow color due to Mn^{2+} emission with respect to BE PL. Inset: enlargement of the main panel between 400 and 800 nm emphasizing the small absorption contribution due to the C−H vibrational modes of the ligand molecules (the measurement is corrected for solvent effects) between 650 and 900 nm and by direct absorption between intragap Mn levels. The inset further highlights the near-complete absence of resonance between the NC absorption tail and the high-energy portion of the Mn PL.

Recently, advancements in Stokes shift engineering of colloidal NCs has boosted the LSC field, enabling the realization of efficient large-area devices based on various classes of semiconductor materials, including heterostructured II−VI or V−VI NCs,[49,71,74−78] NCs doped with metal impurities[75,79] or of ternary I−III−VI composition,[57,80−83] and silicon NCs,[56] in which effective separation between the absorption and emission functions is achieved respectively by

DOI: 10.1021/acsenergylett.7b00701
ACS Energy Lett. 2017, 2, 2368−2377

selective carrier localization in different structural regions of the same particle, by the exploitation of emission mechanisms involving dopant or defect-related intragap states, or, in the case of silicon NCs,[56] the partial forbiddances of the band-edge (BE) transitions due to the indirect nature of the energy gap. Similar to conventional chalcogenide NCs,[49] perovskite NCs feature a very small Stokes shift between their absorption and emission spectra,[6] resulting in strong reabsorption losses for propagation distances as short as a few centimeters.[84] To date, no study on the application of Stokes shift engineered perovskite NCs to LSCs has been reported in the literature.

As a proof-of-concept of utilizing doped perovskite NCs as zero-reabsorption LSC emitters and to assess their compatibility with the radical cell-casting mass polymerization method used for producing optical-grade nanocomposite waveguides, in this work, we fabricate poly(acrylate) LSCs embedded with Mn-doped $CsPbCl_3$ NCs. We specifically chose $CsPbCl_3$ as a host material because, in this system, both the $^6A_1$ singlet ground state and the $^4T_1$ excited triplet state of Mn^{2+} cations are positioned within the forbidden energy gap of the NC host,[42,85] leading to the most effective sensitization of the dopant by the NC host with respect to all other $CsPbX_3$ varieties of both pure and mixed halide compositions.[42] The schematic energy diagram of the doped NC is depicted in Figure 1b, showing the intrinsic BE radiative excitonic transition essentially resonant with the respective absorption and the $^4T_1$ excited state of Mn^{2+}. Crucially for LSC application, the ground ($^6A_1$) and the excited states of Mn^{2+} have different spin multiplicity, resulting in the characteristic vanishingly small extinction coefficient (~1 M^{-1} cm^{-1}) of the spin-forbidden $^6A_1 \rightarrow {}^4T_1$ absorption transition.[86] This leads to the corresponding long-lived $^4T_1 \rightarrow {}^6A_1$ luminescence, indirectly excited by the host semiconductor, to be negligibly affected by reabsorption. We notice that, for our purpose, the eventual presence of some residual excitonic photoluminescence (PL) closely resonant with the optical absorption edge is particularly useful as it enables us to directly compare, in the exact same experimental conditions and on the same material system, the effects of reabsorption on both the dopant emission and the intrinsic BE luminescence, which effectively describes the behavior expected for undoped $CsPbCl_3$ NCs. Light propagation measurements in test-bed one-dimensional liquid LSCs, corroborated by Monte Carlo ray tracing simulations based on the experimental parameters, indicate that the dopant luminescence is essentially unaffected by reabsorption losses, whereas the BE emission undergoes a dramatic (80%) drop due to reabsorption for propagation distances of ~10−15 cm. In order to validate our estimations in a real LSC device, we fabricated and tested nanocomposite waveguides consisting of a mass-polymerized poly(acrylate) matrix incorporating the NCs. Spectroscopic measurements of the NC in toluene solution and embedded in the polymer waveguide indicate that the dopant-related optical properties are fully preserved after the radical polymerization process, thus further demonstrating the suitability of doped perovskite NCs as emitters in plastic nanocomposites potentially applicable, in addition to LSCs, to solid-state lighting or display devices. Finally, light propagation measurements on a proof-of-principle LSC device confirm and extend the observation in the liquid waveguide, showing that the perovskite NC-LSC behaves nearly like an ideal device with essentially no reabsorption or scattering losses.

Synthesis and Optical Properties of Mn-Doped $CsPbCl_3$ NCs. Monodisperse Mn-doped $CsPbCl_3$ NCs were synthesized as described by Protesescu et al.,[6] with addition of $MnCl_2$.

Briefly, 0.1 mmol of $PbCl_2$ and 0.1 mmol of $MnCl_2$, 5 mL of octadecene, 0.5 mL of oleic acid, and 0.5 mL of oleylamine were loaded in a 25 mL three-neck flask and dried under vacuum for 1 h at 120 °C. After degassing, the temperature was raised to 180 °C and 0.4 mL of previously synthesized Cs-oleate (0.4 g of Cs_2CO_3 degassed in 15 mL of octadecene and 1.75 mL of oleic acid at 150 °C) was swiftly injected. Thirty seconds after the injection, the NC solution was quickly cooled down to room temperature with an ice bath.

The NCs were purified via centrifugation (at 3000 rpm for 30 min) twice, followed by redispersion in toluene. As shown in Figure 1c,d, monodisperse and crystalline 8.6 ± 0.6 nm sized NCs were obtained, and inductively coupled plasma optical emission spectroscopy on washed NCs indicated a 3.9% Mn doping. We notice that such a Mn concentration could still be overestimated due to the difficulty in removing the excess Mn ions from the reaction medium completely.[44] A schematic depiction of crystal structure of a $CsPbX_3$ perovskite doped with 5% Mn not considering local changes in crystal structure is reported in the inset of Figure 1c, showing a Mn^{2+} ion in a substitutional Pb site with essentially identical octahedral coordination with six halide atoms. The X-ray diffraction (XRD) pattern reported in Figure 1e indicates a match with cubic $CsPbCl_3$, in agreement with previous studies on Mn-doped $CsPbCl_3$ NCs.[42,44] Figure 1f shows the optical absorption and PL spectrum of the NCs with the characteristic sharp absorption edge at ~395 nm and the respective narrow-line BE PL peaked at ~405 nm, accounting for ~20% of the total emission. The remaining 80% of emitted photons are due to the $^4T_1 \rightarrow {}^6A_1$ optical transition of the Mn^{2+} dopants, giving rise to the characteristic broad peak at ~590 nm (hereafter indicated as Mn^{2+} PL), resulting in a very large ~200 nm (~1 eV) Stokes shift from the absorption edge of the $CsPbCl_3$ host NC.[42,44,85] The PL quantum yield, as measured with an integrating sphere, is $\Phi_{PL,BE}$ = 5 ± 1% for the BE emission and $\Phi_{PL,Mn}$ = 10 ± 2% for the Mn^{2+} PL, in agreement with previous reports.[42] Importantly, the Mn^{2+} PL is nearly completely unaffected by absorption by the NC host, as emphasized in the inset of Figure 1f, where we report enlargement of the absorption spectrum for absorption coefficients between 0 and 5×10^{-2} cm^{-1}. On this expanded scale, it becomes clear that, in agreement with what was observed for Mn-doped ZnSe NCs,[79] the absorption tail on the high-energy portion of the Mn^{2+} PL peak and the small band at ~630 nm, respectively due to the NC host and to Mn^{2+} transitions, are significantly lower than the absorption contribution due to the vibrational modes of the C−H bonds of oleic acid and oleylamine ligands[25] between 650 and 900 nm, which, at this NC concentration (0.08 wt %), are still below 3×10^{-2} cm^{-1}.

Evaluation of Reabsorption Losses: Monte Carlo Simulations and One-Dimensional Liquid LSCs. In order to assess the potential of Mn-doped $CsPbCl_3$ NCs for reabsorption-free LSC by taking into consideration also the effect of stochastic reabsorption and re-emission events in a real device, we performed Monte Carlo ray tracing simulations of light propagation using the experimental absorption and PL spectra reported in Figure 1f. In our simulations, we used the device dimensions (0.25 cm × 0.25 cm × 22 cm) of a one-dimensional liquid test-bed LSC reported later in this work and investigated the evolution of the light output probability for both the BE

DOI: 10.1021/acsenergylett.7b00701
ACS Energy Lett. 2017, 2, 2368−2377

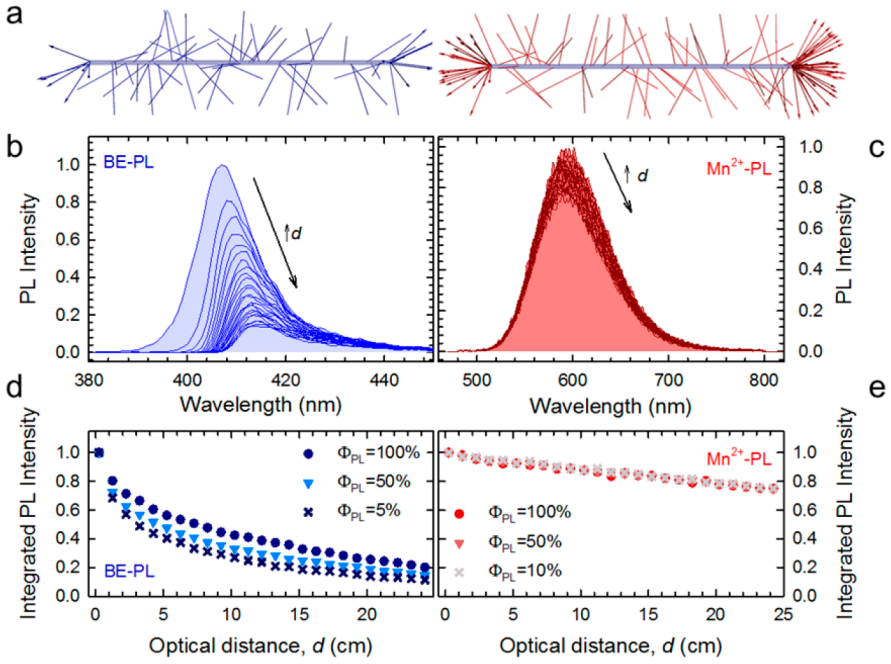

Figure 2. Monte Carlo ray tracing simulations. (a) Visualization of Monte Carlo ray tracing simulations for LSC devices incorporating Mn/$CsPbCl_3$ NCs, highlighting the behavior of the intrinsic BE luminescence (left panel, blue arrows) and of the Mn^{2+} emission (right, red arrows). The device dimensions and NC concentration are the same as those for the one-dimensional waveguide reported in Figure 3 (0.25 × 0.25 × 22 cm^3, 0.08 wt %). Simulated PL spectra due to (b) BE exciton recombination (blue curves) and (c) Mn-related emission (red curves) as a function of increasing optical distance, *d*, between the excitation spot and the edge of the concentrator calculated considering the experimental quantum yields $\Phi_{PL,BE}$ = 5 ± 1% for the BE emission and $\Phi_{PL,Mn}$ = 10 ± 2% for the Mn^{2+} PL. Respective spectrally integrated PL intensities (crosses) vs *d* showing (d) a strong drop of the BE luminescence and (e) near-invariance of the Mn emission intensity. The trends calculated using Φ_{PL} = 50 and 100% are shown for both emissions as triangles and circles, respectively. In (d) and (e), the trends are normalized to their initial value at *d* = 0.

emission and the Mn^{2+} PL, from one of the small 0.25 cm × 0.25 cm LSC edges for an increasingly long optical distance, *d*, from the excitation spot. To decouple the losses due to nonradiative decay and randomization of the propagation direction following reabsorption/re-emission, we performed our calculations using both the experimental values of Φ_{PL} (namely $\Phi_{PL,BE}$ = 5 ± 1% for the BE emission and $\Phi_{PL,Mn}$ = 10 ± 2% for the Mn^{2+} PL) and by considering equal Φ_{PL} for both emissions of 50 and 100%. Panels (a) and (b) in Figure 2, respectively, visualize the Monte Carlo ray tracing simulations for the BE emission and the Mn^{2+} PL calculated using the experimental Φ_{PL} values. The corresponding simulated PL spectra are shown in Figure 2b,c for increasing propagation length, *d*, from *d* = 0.25 to 22 cm. Because of the large overlap with the absorption edge, the BE emission undergoes strong progressive dimming of its high-energy portion, resulting in ∼80% intensity loss in less than a 15 cm optical distance, reaching ∼90% dimming for *d* = 25 cm.

Notably, considering higher emission efficiencies up to $\Phi_{PL,BE}$ = 100% for perfectly emitting NCs, the output probability for the BE PL from the LSC edge increases slightly while still maintaining the strongly negative *d*-dependent trend resulting from the dominant effect of propagation randomization over nonradiative exciton decay. We notice that, with respect to conventional CdSe NCs, showing nearly complete reabsorption in less than a 5 cm propagation distance for nominally identical BE absorbance,[49] the BE emission of perovskite NCs is less affected by reabsorption due to their much narrower excitonic absorption peak,[84] resulting in a sharp cutoff mostly of the high-energy portion of the PL spectrum. Most importantly, the Mn^{2+} PL is essentially unaffected by reabsorption by the NC host, as demonstrated by the invariance of the high-energy spectral tail, whereas the minor decrease of the low-energy portion is mostly due to absorption by the vibrational modes of the ligand molecules, leading to ∼20% intensity drop for *d* as long as 25 cm. In this case, because reabsorption by the NC is essentially absent, the same trend of the light output probability vs *d* is observed for any value of $\Phi_{PL,Mn}$.

On the basis of these promising theoretical predictions, we proceed with experimentally evaluating the reabsorption losses in a one-dimensional liquid waveguide consisting of a 22 cm × 0.25 cm × 0.25 cm quartz cuvette filled with a toluene solution of Mn/$CsPbCl_3$ NCs with the same concentration as the one used for the Monte Carlo simulations shown in Figure 2b–d. The use of a one-dimensional liquid waveguide as a test-bed LSC device[75] is particularly useful in the case of wide-band-gap materials such as chlorine-based perovskites that require UV photoexcitation, which could lead to parasitic emission contributions by the polymer matrix that complicate the data analysis, as described in detail in the next section. In this experiment, the PL spectrum is collected at the edge of the waveguide for increasing spatial separation *d* between the excitation spot and the LSC edge, as schematically depicted in Figure 3a. The PL spectra for both the BE and the Mn-related emissions at increasing *d* are shown in Figure 3b, showing close resemblance of the theoretical predictions reported in Figure 2b,c. Specifically, the BE luminescence undergoes progressive quenching of its high-energy tail due to reabsorption, resulting in a strong ∼80% intensity drop for *d* ≈ 10 cm. On the other

DOI: 10.1021/acsenergylett.7b00701
ACS Energy Lett. 2017, 2, 2368−2377

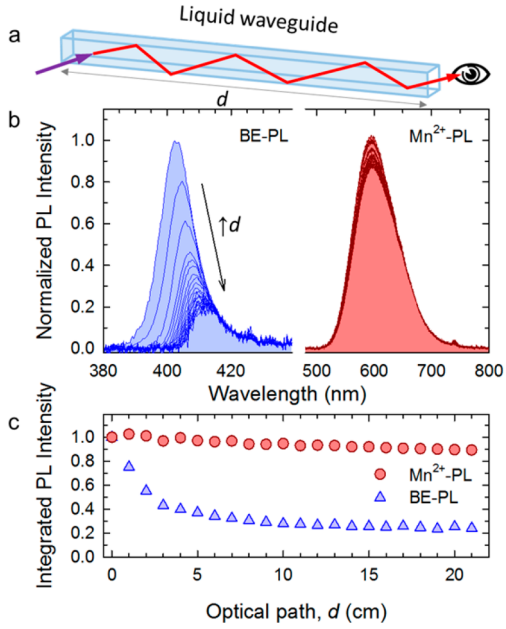

Figure 3. Light propagation experiments. (a) Schematic depiction of the experimental configuration used in the light propagation measurements on liquid test-bed LSCs with Mn/$CsPbCl_3$ NCs. (b) PL spectra due to BE exciton recombination (blue curves) and Mn-related emission (red curves) of the same NCs collected at increasing optical distance, *d*, between the excitation spot and the edge of a one-dimensional liquid waveguide (excitation wavelength = 395 nm; dimensions: 0.25 × 0.25 × 20 cm^3; NC concentration: 0.08 wt %). (c) Respective spectrally integrated PL intensities vs *d* showing near-invariance of the Mn emission intensity and a strong drop of the BE luminescence in accordance with the Monte Carlo theoretical predictions.

hand, in agreement with the theoretical simulations, the Mn^{2+} PL is nearly unaffected by reabsorption, and its dimming is only ∼15% for optical distances as long as 22 cm.

Mass Polymerized Reabsorption-Free Perovskite LSCs. After assessing the potential of Mn-doped $CsPbCl_3$ perovskite NCs as reabsorption-free emitters for LSCs, we proceed with the practical demonstration of a polymer-based LSC incorporating the NCs. With this aim, we fabricated a proof-of-principle LSC device by radical mass polymerization of an 80:20 wt % mixture of methyl methacrylate (MMA) and lauryl methacrylate (LMA) doped with NCs. The choice of poly(methyl methacrylate) (PMMA) as the main waveguide material is dictated by its excellent optical properties, high resistance to exposure to UV light, and various chemical treatments, as well as excellent performance in all-weather conditions. For these reasons, PMMA is widely used in construction as a lightweight window material and in optics for fabricating lenses and prisms as well as in optical fibers. On the other hand, LMA has long alkyl side chains that display dynamics resembling those of liquids. Exposure of the monomer mixture to 365 nm UV light in the presence of the radical photoinitiator (IRGACURE 651; 1% w/w) results in mass polymerization of a random copolymer[87] unaffected by macroscopic phase segregation that could be detrimental to the optical transport properties of the waveguide due to scattering. Notably, because the polar methacrylate backbone and the nonpolar alkyl side chains of LMA are incompatible but connected by a covalent bond, the polymer bulk is phase separated at the nanoscopic level,[88] which provides the NCs with a local environment that is very similar to that of octadecene or analogous solvents[89] used in the NC synthesis. This specially designed near-native polymeric environment largely improves the miscibility of the NCs with the monomer mixture, leading to a scattering-free nanocomposite.

The fabrication procedure consists of initial wetting of the NCs in a small volume of LMA monomer for 3 h to ensure fine dispersion of the individual particles. The monomer−NC mixture is then added to a large volume of MMA together with the radical photoinitiator. With respect to the polymerization routes of pure LMA used in previous studies, no cross-linking agent was added to the mixture as the dominant PMMA fraction ensures mechanical stability of the nanocomposite at room temperature (see Figures S1 and S2).

Figure 4a reports two photographs of a fabricated LSC with dimensions of 25 cm × 20 cm × 0.5 cm comprising 0.03 wt % NCs under ambient and 365 nm UV illumination, showing yellow luminescence, of qualitatively comparable color as the toluene solution shown in the inset of Figure 1f, emerging mostly from the slab edges with minor emission from its surfaces, suggesting that light scattering in this device is particularly low. The concentration of NC was chosen in order to achieve ∼70% optical absorption of band gap radiation. Increasing it further does not significantly increase the absorption but could introduce scattering losses due to NC aggregation. The picture taken under ambient illumination highlights the high optical quality of the LSC waveguide that appears nearly transparent, as expected given the very sharp absorption edge of the NCs at 395 nm. In order to experimentally quantify the scattering losses of our LSC at the emission wavelength of the Mn^{2+} PL, we performed light propagation experiments using a collimated laser source at 633 nm entering the device from one edge and collecting the light intensity escaping from the LSC faces. The results, shown in Figure 4b, reveal that the light output undergoes ∼20% drop for a propagation distance of 25 cm, in agreement with the absorption by the polymer matrix ($\alpha \approx 1 \times 10^{-2}$ cm^{-1}), thus confirming that the scattering losses for the Mn^{2+} PL are essentially negligible. Accordingly, the attenuation of the laser light vs *d* matches well the trend calculated using the Lambert−Beer equation for linear propagation along the waveguide. One further critical step for the realization of poly(acrylate) LSCs based on perovskite NCs is the preservation of their spectral properties and PL efficiency after the mass polymerization procedure involving highly reactive radical initiators. In order to test this aspect, we conducted side-by-side spectroscopic measurements on the NCs in solution and embedded in the polymer waveguide. The emission spectrum of the BE luminescence and Mn^{2+} PL in both the native toluene solution and in the P(MMA/LMA) nanocomposite collected in reflection geometry to minimize reabsorption effects are reported in Figure 4c, showing essentially no differences between the two conditions, which demonstrates that the polymerization procedure does not modify the spectral properties of the NCs. The same figure also shows the absorption spectrum of the nanocomposite (gray line), in direct comparison with the absorption spectrum of a P(MMA/LMA) slab of identical thickness and composition but without the NCs (light blue pattern). The first excitonic feature of the NCs is clearly distinguishable at 395 nm, in agreement with the spectrum in toluene solution shown in Figure 1f. Both the bare slab and the nanocomposite show a steep edge at about 390 nm followed by a weak tail at longer wavelengths likely due to low-

DOI: 10.1021/acsenergylett.7b00701
ACS Energy Lett. 2017, 2, 2368−2377

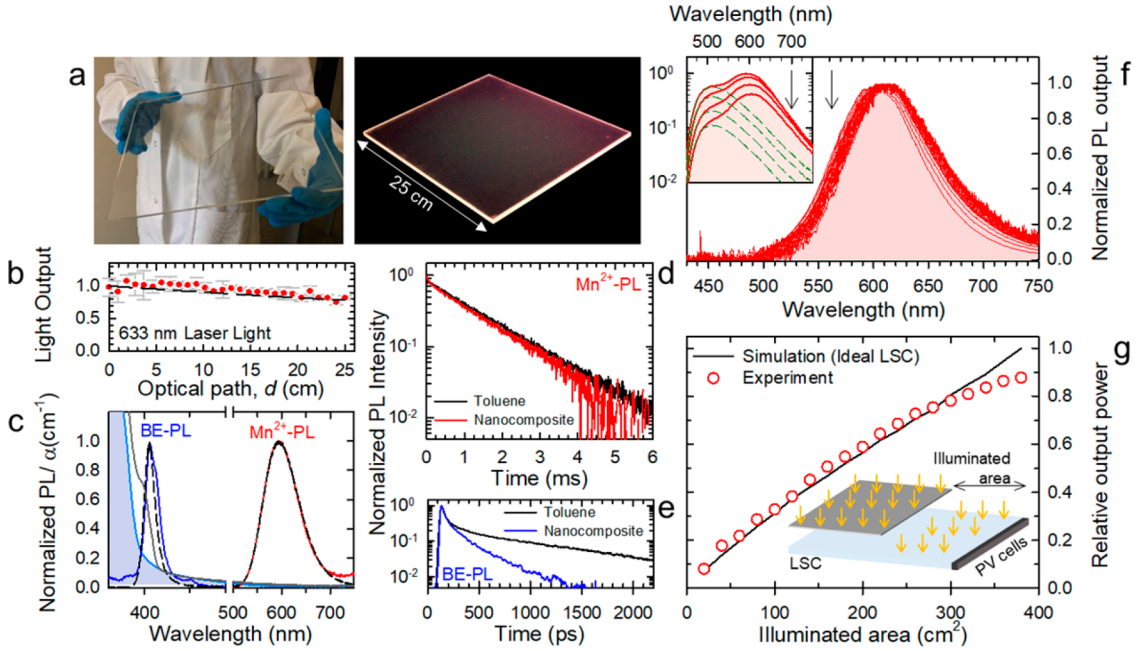

Figure 4. Polymer nanocomposites and reabsorption-free LSCs. (a) Photograph of an LSC comprising Mn/$CsPbCl_3$ NCs (LSC dimensions: 25 cm × 20 cm × 0.5 cm; NC concentration 0.03 wt %) under ambient (left) and UV illumination (365 nm, right). (b) Intensity of 633 nm laser light linearly propagating inside of the LSC in (a) as a function of propagation path *d*. The error bars are the standard deviation calculated over five repetitive measurements. The light intensity versus *d* calculated using the Lambert−Beer equation for linear propagation (absorption coefficient α (633 nm) = 1×10^{-2} cm^{-1}) is reported as a black dashed line. (c) PL spectra of the BE and Mn^{2+} PL of Mn/$CsPbCl_3$ NCs excited at 395 nm in photopolymerized P(MMA/LMA) (blue and red lines, respectively) and in toluene solution (dashed black lines). The spectrally resolved absorption coefficient of the LSC is shown as a gray line in direct comparison to the spectrum of a pure P(MMA/LMA) slab (light blue shaded area), showing the absorption edge of the polymer absorption at ∼395 nm and the long tail due to the structural defects responsible for the greenish PL. The PL decay curves collected at (d) 600 nm for the Mn^{2+} PL for NCs and (e) 405 nm for the BE emission in toluene solution (black lines) and embedded in the P(MMA/LMA) matrix (red and blue lines, respectively). (f) Normalized PL spectra (excitation at 395 nm) collected at the edge of the LSC when the excitation spot is located at increasing distances *d* from 0 to 25 cm from the edge (as indicated by the black arrow) after subtraction of the corresponding emission contribution by the polymer matrix. The raw PL data under site-selective excitation are shown in the inset; the red lines are excited at 395 nm and show contribution of both the polymer and the NCs. The green dashed lines are excited in the low-energy tail of the polymer defects at 410 nm and are due exclusively to the polymer matrix. The black arrow indicates increasing *d*. (g) Relative optical output power measured from c-Si PVs coupled to one perimeter edge of the NC-LSC as a function of the device area illuminated by a calibrated solar simulator (1.5 AM Global, circles). The theoretical trend obtained through Monte Carlo ray tracing simulation of an ideal LSC with no scattering or reabsorption losses is reported as a black curve. The inset shows the schematic depiction of the experimental configuration.

energy-absorbing structural defects and minor residual scattering of UV light. As shown later in this section, optical excitation of these states at 410 nm leads to a parasitic greenish PL that is strongly reabsorbed by the composite. More importantly, time-resolved PL measurements show that the decay dynamics of the Mn^{2+} PL are identical in toluene and in the nanocomposite (Figure 4d), indicating that the quantum efficiency of the dopant emission is unaffected by exposure to the radical photoinitiators. In contrast, the BE PL shows acceleration of its time trace in the nanocomposite with respect to toluene (Figure 4e), which suggests that BE excitons are more subject than the dopant states to surface reactions, which activate nonradiative processes competitive to radiative decay, in agreement with recent spectroelectrochemical results.[41] Nevertheless, the acceleration of the BE dynamics seems to affect only the slow portion of the decay curve, which accounts for only ∼20% of the total PL, thus suggesting that most of the emission efficiency is retained also for the BE PL upon incorporation in the nanocomposite, as previously qualitatively suggested for undoped perovskite NCs.[6] Because of the resonance between the excitonic absorption by the NCs and the low-energy tail of the polymer slab shown in Figure 4c, an accurate estimation of the number of photons absorbed by the NCs is not experimentally accessible in this system, which prevents us from measuring the absolute PL efficiency of the NCs in the nanocomposite.

Next, we proceeded by confirming the absence of reabsorption effects on the Mn^{2+} PL also in our polymer-based LSC device. With this aim, we collected the PL spectrum from one of the slab edges (20 × 0.5 cm^2) using 395 nm laser excitation positioned at different distances, *d*, from the waveguide edge, similar to the light propagation experiments on the one-dimensional liquid LSC reported in Figure 3. As anticipated above, in this excitation condition, the polymer waveguide exhibits a parasitic greenish emission at ∼500 nm (inset of Figure 4f) likely arising from polymer defects responsible for the absorption tail of both bare and NC-containing P(MMA/LMA) slabs. Such PL is, however, strongly reabsorbed by the matrix, resulting in ∼80% drop in a less than 3 cm propagation distance. The decay dynamics of this luminescence is on the same time scale as the Mn^{2+} PL, which prevents the use of time-gated techniques for decoupling the two emission components. In order to extract the trend of the Mn^{2+} PL as much as possible unaffected by this spurious luminescence, we therefore performed side-by-side PL measurements under spectrally selective excitation conditions

DOI: 10.1021/acsenergylett.7b00701
ACS Energy Lett. 2017, 2, 2368−2377

for the polymer and the NC's PL at identical values of d. Specifically, we tuned the emission of a Ti:sapphire laser at 395 nm to excite mostly the NCs and at 410 nm, which is below the absorption edge of the NCs, to selectively pump the polymer matrix. In this way, we obtained the set of spectra reported in the inset of Figure 4f, from which, by subtraction, we extracted the emission spectra of the Mn^{2+} PL as a function of d. In Figure 4f, we report the normalized spectra of the Mn^{2+} PL for d = 0−25 cm obtained through the procedure described above, showing minor spectral modification in qualitative agreement with the data on the one-dimensional liquid waveguide shown in Figure 3.

One final confirmation of the absence of reabsorption and scattering losses for the Mn^{2+} PL in our LSCs is that all portions of the device surface contribute nearly equally to its total power output. To highlight this behavior, in Figure 4g, we show the relative output power extracted from one of the LSC edges (20 × 0.5 cm^2) measured by coupling calibrated c-Si solar cells to one slab edge and by progressively exposing increasingly larger portions of the LSC area to the solar simulator. The trend calculated by Monte Carlo ray tracing simulation for an ideal scattering- and reabsorption-free LSC of identical dimensions embedding emitters with the same Φ_{PL} as the Mn^{2+} PL, for which the power output is determined exclusively by the numeric aperture of the illuminated area, is also reported in Figure 4g for direct comparison with the experimental data. The calculated curve matches well the experimental behavior for illumination fractions as large as ∼80%, indicating that suppression of reabsorption in Mn/$CsPbCl_3$ perovskite NCs is effective in rendering the device behavior close to ideal.[56] This match between theory and experiments further confirms that the effect of the parasitic polymer emission on the total device light output is negligible, as expected based on its strong reabsorption observed for very short optical distances (inset of Figure 4f).

Despite the nearly complete suppression of reabsorption for the dopant emission, we highlight that Mn/$CsPbCl_3$ perovskite NCs are not directly suitable for the fabrication of highly efficient LSCs because of both their relatively low emission efficiency and their wide energy gap, which results in their absorption edge being positioned in the near-UV end of the visible spectrum (395 nm, Figure 1f). This limits the light-harvesting capability by the NCs to below ∼5% of the solar spectrum and results in significant overlap with the absorption tail of the polymer matrix, which further lowers the intensity of incident light available for NC excitation. As a result, the optical power efficiency of our LSC, measured by illuminating the device perpendicular to its top surface using a calibrated solar simulator with power density I = 100 mW/cm^2 (1.5 AM Global) and collecting the guided luminescence by calibrated c-Si solar cells index matched to the perimeter edges of the slab, is $\eta = P_{OUT}/P_{IN} < 0.5\%$ (including the minor contributions of the BE and polymer emission), where P_{OUT} is the luminous power collected by the solar cells and P_{IN} is the solar power incident on the LSC surface. With regard to optimization of the PL quantum efficiency, strategies are being investigated for suppressing nonradiative carrier trapping in localized defects. For example, Kosher et al.[30] recently demonstrated trap-free perovskite NCs by postsynthetic treatment with thiocyanate, resulting in unitary emission efficiency from undoped $CsPbBr_3$ NCs. Such an approach has not yet been applied to doped perovskite NCs, and in case of success, it could boost their efficiency to values suitable for highly performing LSCs. Extension of the solar coverage by the NCs will require means to lower the energy gap of the NC host, and improved doping strategies will be concomitantly needed for ensuring a sufficiently wide Stokes shift to suppress reabsorption. Given the small effect of carrier confinement on the electronic properties of perovskite NCs, size tuning is not sufficient to reach extended solar coverage with chlorine-based perovskites, and other formulations are therefore required. Manganese, in turn, is a valuable dopant for proving the potential of these structures for photon management applications, but its d−d optical transition at ∼600 nm limits the maximum spectral coverage to the green portion of the solar spectrum. $CsPbI_3$ NCs could, in principle, be suitable as broad-band absorbing hosts to nearly 700 nm,[6,84] provided that strategies are found for their stabilization and for the incorporation of impurities capable of activating efficient Stokes shifted near-IR luminescence. A further possibility could be the use of $CsSnX_3$ perovskite NCs recently demonstrated by Jellicoe et al.,[90] showing broad-band optical absorption and Stokes shifted PL likely due to the involvement of localized defect states in the exciton recombination mechanisms. These systems would have the additional advantage of having a Pb-free composition, but their current PL quantum yield would require optimization to be suitable for efficient LSCs. Another possibility for removing the potential environmental risks associated with Pb could be to engineer the Stokes shift of recently reported cesium bismuth halide perovskites.[91]

To date, doping of perovskite NCs, as well as their Stokes shift engineering, is still at the embryo stage, and novel approaches are continuously appearing in the literature, suggesting that perovskite NCs with optimized performances specifically designed for advanced photon management technologies could be achieved in the short term.

In conclusion, we have demonstrated the suitability of doped perovskite NCs as nearly zero reabsorption emitters for LSCs. Light propagation measurements in both test-bed one-dimensional waveguides and poly(acrylate) concentrators, corroborated by Monte Carlo ray tracing simulations, indicate that the dopant PL is nearly completely unaffected by reabsorption losses by the NC host and the only effects are due to resonance with the vibrational modes of the ligand molecules leading to a small 15% optical loss for propagation lengths as long as 20 cm. Polymer-based LSCs were fabricated using the radical mass polymerization procedure of a mixture of MMA and LMA to simultaneously ensure thermal and mechanical stability and optimal compatibility of the NCs, resulting in high optical quality waveguides, in which scattering losses are less than the weak reabsorption by the matrix material ($\alpha \approx 1 \times 10^{-2}$ cm^{-1}). Importantly, time-resolved PL measurements indicate that the dopant-related PL of the NCs is fully preserved. Accordingly, the LSC behaves closely to an ideal device, in which all portions of the illuminated area contribute equally to the total optical power. These proof-of-principle results demonstrate the potential of doped perovskite NCs for LSC-based BIPV technologies as well as for other photon management applications relying on low-attenuation long-range optical wave guiding.

■ ASSOCIATED CONTENT

Supporting Information

The Supporting Information is available free of charge on the ACS Publications website at DOI: 10.1021/acsenergylett.7b00701.

DOI: 10.1021/acsenergylett.7b00701
ACS Energy Lett. 2017, 2, 2368−2377

Differential scanning calorimetry, mechanical properties, and experimental methods (PDF)

AUTHOR INFORMATION

Corresponding Authors

*E-mail: franco.meinardi@mater.unimib.it. Phone:+39 02 6448 5181 (F.M.).
*E-mail: sergio.brovelli@unimib.it. Phone:+39 02 6448 5027 (S.B.).
*E-mail: liberato.manna@iit.it. Phone: +39 010 71781 502 (L.M.).

ORCID

Sungwook Park: 0000-0002-2310-4836
Liberato Manna: 0000-0003-4386-7985
Sergio Brovelli: 0000-0002-5993-855X

Notes

The authors declare no competing financial interest.

ACKNOWLEDGMENTS

We thank Professor Roberto Simonutti for valuable insights into the mechanical and thermal behavior of the nanocomposite and Dr. Norberto Manfredi and Professor Maurizio Acciarri of the MIB-SOLAR Laboratory for technical assistance in quantitative studies of solar concentration. L.M., Q.A.A., and Z.D. acknowledge the European Union seventh Framework Programme under Grant Agreement No. 614897 (ERC Consolidator Grant TRANS-NANO). S.P. acknowledges the Basic Science Research Program through the National Research Foundation of Korea (NRF) funded by the Ministry of Education (NRF-2014R1A1A2009367).

REFERENCES

(1) Sichert, J. A.; Tong, Y.; Mutz, N.; Vollmer, M.; Fischer, S.; Milowska, K. Z.; García Cortadella, R.; Nickel, B.; Cardenas-Daw, C.; Stolarczyk, J. K.; et al. Quantum Size Effect in Organometal Halide Perovskite Nanoplatelets. *Nano Lett.* **2015**, *15*, 6521−6527.

(2) Zhang, D.; Eaton, S. W.; Yu, Y.; Dou, L.; Yang, P. Solution-Phase Synthesis of Cesium Lead Halide Perovskite Nanowires. *J. Am. Chem. Soc.* **2015**, *137*, 9230−9233.

(3) Zhang, F.; Zhong, H.; Chen, C.; Wu, X.-g.; Hu, X.; Huang, H.; Han, J.; Zou, B.; Dong, Y. Brightly Luminescent and Color-Tunable Colloidal $CH_3NH_3PbX_3$ (X = Br, I, Cl) Quantum Dots: Potential Alternatives for Display Technology. *ACS Nano* **2015**, *9*, 4533−4542.

(4) Akkerman, Q. A.; D'Innocenzo, V.; Accornero, S.; Scarpellini, A.; Petrozza, A.; Prato, M.; Manna, L. Tuning the Optical Properties of Cesium Lead Halide Perovskite Nanocrystals by Anion Exchange Reactions. *J. Am. Chem. Soc.* **2015**, *137*, 10276−10281.

(5) Akkerman, Q. A.; Motti, S. G.; Srimath Kandada, A. R.; Mosconi, E.; D'Innocenzo, V.; Bertoni, G.; Marras, S.; Kamino, B. A.; Miranda, L.; De Angelis, F.; et al. Solution Synthesis Approach to Colloidal Cesium Lead Halide Perovskite Nanoplatelets with Monolayer-Level Thickness Control. *J. Am. Chem. Soc.* **2016**, *138*, 1010−1016.

(6) Protesescu, L.; Yakunin, S.; Bodnarchuk, M. I.; Krieg, F.; Caputo, R.; Hendon, C. H.; Yang, R. X.; Walsh, A.; Kovalenko, M. V. Nanocrystals of Cesium Lead Halide Perovskites ($CsPbX_3$, X = Cl, Br, and I): Novel Optoelectronic Materials Showing Bright Emission with Wide Color Gamut. *Nano Lett.* **2015**, *15*, 3692−3696.

(7) He, X.; Qiu, Y.; Yang, S. Fully-Inorganic Trihalide Perovskite Nanocrystals: A New Research Frontier of Optoelectronic Materials. *Adv. Mater.* **2017**, *29*, 1700775.

(8) Akkerman, Q. A.; Gandini, M.; Di Stasio, F.; Rastogi, P.; Palazon, F.; Bertoni, G.; Ball, J. M.; Prato, M.; Petrozza, A.; Manna, L. Strongly Emissive Perovskite Nanocrystal Inks for High-Voltage Solar Cells. *Nat. Energy* **2016**, *2*, 16194.

(9) Swarnkar, A.; Marshall, A. R.; Sanehira, E. M.; Chernomordik, B. D.; Moore, D. T.; Christians, J. A.; Chakrabarti, T.; Luther, J. M. Quantum Dot−Induced Phase Stabilization of A-$CsPbI_3$ Perovskite for High-Efficiency Photovoltaics. *Science* **2016**, *354*, 92−95.

(10) Zhang, J.; Wang, Q.; Zhang, X.; Jiang, J.; Gao, Z.; Jin, Z.; Liu, S. High-Performance Transparent Ultraviolet Photodetectors Based on Inorganic Perovskite $CsPbCl_3$ Nanocrystals. *RSC Adv.* **2017**, *7*, 36722−36727.

(11) Zhang, X.; Wang, Q.; Jin, Z.; Zhang, J.; Liu, S. Stable Ultra-Fast Broad-Bandwidth Photodetectors Based on α-$CsPbI_3$ Perovskite and $NaYF_4$:Yb,Er Quantum Dots. *Nanoscale* **2017**, *9*, 6278−6285.

(12) Li, G.; Rivarola, F. W. R.; Davis, N. J. L. K.; Bai, S.; Jellicoe, T. C.; de la Peña, F.; Hou, S.; Ducati, C.; Gao, F.; Friend, R. H.; et al. Highly Efficient Perovskite Nanocrystal Light-Emitting Diodes Enabled by a Universal Crosslinking Method. *Adv. Mater.* **2016**, *28*, 3528−3534.

(13) Palazon, F.; Di Stasio, F.; Akkerman, Q. A.; Krahne, R.; Prato, M.; Manna, L. Polymer-Free Films of Inorganic Halide Perovskite Nanocrystals as UV-to-White Color-Conversion Layers in Leds. *Chem. Mater.* **2016**, *28*, 2902−2906.

(14) Zhang, X.; Lin, H.; Huang, H.; Reckmeier, C.; Zhang, Y.; Choy, W. C. H.; Rogach, A. L. Enhancing the Brightness of Cesium Lead Halide Perovskite Nanocrystal Based Green Light-Emitting Devices through the Interface Engineering with Perfluorinated Ionomer. *Nano Lett.* **2016**, *16*, 1415−1420.

(15) Zhang, X.; Xu, B.; Zhang, J.; Gao, Y.; Zheng, Y.; Wang, K.; Sun, X. W. All-Inorganic Perovskite Nanocrystals for High-Efficiency Light Emitting Diodes: Dual-Phase $CsPbBr_3$-$CsPb_2Br_5$ Composites. *Adv. Funct. Mater.* **2016**, *26*, 4595−4600.

(16) Yao, E.-P.; Yang, Z.; Meng, L.; Sun, P.; Dong, S.; Yang, Y.; Yang, Y. High-Brightness Blue and White Leds Based on Inorganic Perovskite Nanocrystals and Their Composites. *Adv. Mater.* **2017**, *29*, 1606859.

(17) Chiba, T.; Hoshi, K.; Pu, Y.-J.; Takeda, Y.; Hayashi, Y.; Ohisa, S.; Kawata, S.; Kido, J. High-Efficiency Perovskite Quantum-Dot Light-Emitting Devices by Effective Washing Process and Interfacial Energy Level Alignment. *ACS Appl. Mater. Interfaces* **2017**, *9*, 18054−18060.

(18) Congreve, D. N.; Weidman, M. C.; Seitz, M.; Paritmongkol, W.; Dahod, N. S.; Tisdale, W. A. Tunable Light-Emitting Diodes Utilizing Quantum-Confined Layered Perovskite Emitters. *ACS Photonics* **2017**, *4*, 476−481.

(19) Eaton, S. W.; Lai, M.; Gibson, N. A.; Wong, A. B.; Dou, L.; Ma, J.; Wang, L.-W.; Leone, S. R.; Yang, P. Lasing in Robust Cesium Lead Halide Perovskite Nanowires. *Proc. Natl. Acad. Sci. U. S. A.* **2016**, *113*, 1993−1998.

(20) Xu, Y.; Chen, Q.; Zhang, C.; Wang, R.; Wu, H.; Zhang, X.; Xing, G.; Yu, W. W.; Wang, X.; Zhang, Y.; et al. Two-Photon-Pumped Perovskite Semiconductor Nanocrystal Lasers. *J. Am. Chem. Soc.* **2016**, *138*, 3761−3768.

(21) Yakunin, S.; Protesescu, L.; Krieg, F.; Bodnarchuk, M. I.; Nedelcu, G.; Humer, M.; De Luca, G.; Fiebig, M.; Heiss, W.; Kovalenko, M. V. Low-Threshold Amplified Spontaneous Emission and Lasing from Colloidal Nanocrystals of Caesium Lead Halide Perovskites. *Nat. Commun.* **2015**, *6*, 8056.

(22) Brennan, M. C.; Zinna, J.; Kuno, M. Existence of a Size-Dependent Stokes Shift in Cspbbr3 Perovskite Nanocrystals. *ACS Energy Lett.* **2017**, *2*, 1487−1488.

(23) Bekenstein, Y.; Koscher, B. A.; Eaton, S. W.; Yang, P.; Alivisatos, A. P. Highly Luminescent Colloidal Nanoplates of Perovskite Cesium Lead Halide and Their Oriented Assemblies. *J. Am. Chem. Soc.* **2015**, *137*, 16008−16011.

(24) Shamsi, J.; Dang, Z.; Bianchini, P.; Canale, C.; Di Stasio, F.; Brescia, R.; Prato, M.; Manna, L. Colloidal Synthesis of Quantum Confined Single Crystal $CsPbBr_3$ Nanosheets with Lateral Size Control up to the Micrometer Range. *J. Am. Chem. Soc.* **2016**, *138*, 7240−7243.

(25) De Roo, J.; Ibáñez, M.; Geiregat, P.; Nedelcu, G.; Walravens, W.; Maes, J.; Martins, J. C.; Van Driessche, I.; Kovalenko, M. V.; Hens,

DOI: 10.1021/acsenergylett.7b00701
ACS Energy Lett. 2017, 2, 2368−2377

Z. Highly Dynamic Ligand Binding and Light Absorption Coefficient of Cesium Lead Bromide Perovskite Nanocrystals. *ACS Nano* **2016**, *10*, 2071−2081.
(26) Huang, H.; Chen, B.; Wang, Z.; Hung, T. F.; Susha, A. S.; Zhong, H.; Rogach, A. L. Water Resistant $CsPbX_3$ Nanocrystals Coated with Polyhedral Oligomeric Silsesquioxane and Their Use as Solid State Luminophores in All-Perovskite White Light-Emitting Devices. *Chem. Sci.* **2016**, *7*, 5699−5703.
(27) Kim, Y.; Yassitepe, E.; Voznyy, O.; Comin, R.; Walters, G.; Gong, X.; Kanjanaboos, P.; Nogueira, A. F.; Sargent, E. H. Efficient Luminescence from Perovskite Quantum Dot Solids. *ACS Appl. Mater. Interfaces* **2015**, *7*, 25007−25013.
(28) Palazon, F.; Almeida, G.; Akkerman, Q. A.; De Trizio, L.; Dang, Z.; Prato, M.; Manna, L. Changing the Dimensionality of Cesium Lead Bromide Nanocrystals by Reversible Postsynthesis Transformations with Amines. *Chem. Mater.* **2017**, *29*, 4167.
(29) Zhang, X.; Lv, L.; Ji, L.; Guo, G.; Liu, L.; Han, D.; Wang, B.; Tu, Y.; Hu, J.; Yang, D.; et al. Self-Assembly of One-Dimensional Nanocrystal Superlattice Chains Mediated by Molecular Clusters. *J. Am. Chem. Soc.* **2016**, *138*, 3290−3293.
(30) Koscher, B. A.; Swabeck, J. K.; Bronstein, N. D.; Alivisatos, A. P. Essentially Trap-Free $CsPbBr_3$ Colloidal Nanocrystals by Postsynthetic Thiocyanate Surface Treatment. *J. Am. Chem. Soc.* **2017**, *139*, 6566−6569.
(31) Castañeda, J. A.; Nagamine, G.; Yassitepe, E.; Bonato, L. G.; Voznyy, O.; Hoogland, S.; Nogueira, A. F.; Sargent, E. H.; Cruz, C. H. B.; Padilha, L. A. Efficient Biexciton Interaction in Perovskite Quantum Dots under Weak and Strong Confinement. *ACS Nano* **2016**, *10*, 8603−8609.
(32) Fu, M.; Tamarat, P.; Huang, H.; Even, J.; Rogach, A. L.; Lounis, B. Neutral and Charged Exciton Fine Structure in Single Lead Halide Perovskite Nanocrystals Revealed by Magneto-Optical Spectroscopy. *Nano Lett.* **2017**, *17*, 2895−2901.
(33) Makarov, N. S.; Guo, S.; Isaienko, O.; Liu, W.; Robel, I.; Klimov, V. I. Spectral and Dynamical Properties of Single Excitons, Biexcitons, and Trions in Cesium−Lead-Halide Perovskite Quantum Dots. *Nano Lett.* **2016**, *16*, 2349−2362.
(34) Park, Y.-S.; Guo, S.; Makarov, N. S.; Klimov, V. I. Room Temperature Single-Photon Emission from Individual Perovskite Quantum Dots. *ACS Nano* **2015**, *9*, 10386−10393.
(35) Rainò, G.; Nedelcu, G.; Protesescu, L.; Bodnarchuk, M. I.; Kovalenko, M. V.; Mahrt, R. F.; Stöferle, T. Single Cesium Lead Halide Perovskite Nanocrystals at Low Temperature: Fast Single-Photon Emission, Reduced Blinking, and Exciton Fine Structure. *ACS Nano* **2016**, *10*, 2485−2490.
(36) Swarnkar, A.; Chulliyil, R.; Ravi, V. K.; Irfanullah, M.; Chowdhury, A.; Nag, A. Colloidal $CsPbBr_3$ Perovskite Nanocrystals: Luminescence Beyond Traditional Quantum Dots. *Angew. Chem., Int. Ed.* **2015**, *54*, 15424−15428.
(37) Tian, Y.; Merdasa, A.; Peter, M.; Abdellah, M.; Zheng, K.; Ponseca, C. S.; Pullerits, T.; Yartsev, A.; Sundström, V.; Scheblykin, I. G. Giant Photoluminescence Blinking of Perovskite Nanocrystals Reveals Single-Trap Control of Luminescence. *Nano Lett.* **2015**, *15*, 1603−1608.
(38) Diroll, B. T.; Nedelcu, G.; Kovalenko, M. V.; Schaller, R. D. High-Temperature Photoluminescence of $CsPbX_3$ (X = Cl, Br, I) Nanocrystals. *Adv. Funct. Mater.* **2017**, *27*, 1606750.
(39) Liu, G.; Kong, L.; Gong, J.; Yang, W.; Mao, H.-k.; Hu, Q.; Liu, Z.; Schaller, R. D.; Zhang, D.; Xu, T. Pressure-Induced Bandgap Optimization in Lead-Based Perovskites with Prolonged Carrier Lifetime and Ambient Retainability. *Adv. Funct. Mater.* **2017**, *27*, 1604208.
(40) Wu, K.; Liang, G.; Shang, Q.; Ren, Y.; Kong, D.; Lian, T. Ultrafast Interfacial Electron and Hole Transfer from $CsPbBr_3$ Perovskite Quantum Dots. *J. Am. Chem. Soc.* **2015**, *137*, 12792−12795.
(41) Lorenzon, M.; Sortino, L.; Akkerman, Q.; Accornero, S.; Pedrini, J.; Prato, M.; Pinchetti, V.; Meinardi, F.; Manna, L.; Brovelli, S. Role of Nonradiative Defects and Environmental Oxygen on Exciton Recombination Processes in $CsPbBr_3$ Perovskite Nanocrystals. *Nano Lett.* **2017**, *17*, 3844−3853.
(42) Liu, W.; Lin, Q.; Li, H.; Wu, K.; Robel, I.; Pietryga, J. M.; Klimov, V. I. Mn^{2+}-Doped Lead Halide Perovskite Nanocrystals with Dual-Color Emission Controlled by Halide Content. *J. Am. Chem. Soc.* **2016**, *138*, 14954−14961.
(43) Mir, W. J.; Jagadeeswararao, M.; Das, S.; Nag, A. Colloidal Mn-Doped Cesium Lead Halide Perovskite Nanoplatelets. *ACS Energy Lett.* **2017**, *2*, 537−543.
(44) Parobek, D.; Roman, B. J.; Dong, Y.; Jin, H.; Lee, E.; Sheldon, M.; Son, D. H. Exciton-to-Dopant Energy Transfer in Mn-Doped Cesium Lead Halide Perovskite Nanocrystals. *Nano Lett.* **2016**, *16*, 7376−7380.
(45) Guria, A. K.; Dutta, S. K.; Adhikari, S. D.; Pradhan, N. Doping Mn^{2+} in Lead Halide Perovskite Nanocrystals: Successes and Challenges. *ACS Energy Lett.* **2017**, *2*, 1014−1021.
(46) van der Stam, W.; Geuchies, J. J.; Altantzis, T.; van den Bos, K. H. W.; Meeldijk, J. D.; Van Aert, S.; Bals, S.; Vanmaekelbergh, D.; de Mello Donega, C. Highly Emissive Divalent-Ion-Doped Colloidal $CsPb_{1-x}M_xBr_3$ Perovskite Nanocrystals through Cation Exchange. *J. Am. Chem. Soc.* **2017**, *139*, 4087−4097.
(47) Begum, R.; Parida, M. R.; Abdelhady, A. L.; Murali, B.; Alyami, N. M.; Ahmed, G. H.; Hedhili, M. N.; Bakr, O. M.; Mohammed, O. F. Engineering Interfacial Charge Transfer in $CsPbBr_3$ Perovskite Nanocrystals by Heterovalent Doping. *J. Am. Chem. Soc.* **2017**, *139*, 731−737.
(48) Brovelli, S.; Schaller, R. D.; Crooker, S. A.; García-Santamaría, F.; Chen, Y.; Viswanatha, R.; Hollingsworth, J. A.; Htoon, H.; Klimov, V. I. Nano-Engineered Electron-Hole Exchange Interaction Controls Exciton Dynamics in Core-Shell Semiconductor Nanocrystals. *Nat. Commun.* **2011**, *2*, 280.
(49) Meinardi, F.; Colombo, A.; Velizhanin, K. A.; Simonutti, R.; Lorenzon, M.; Beverina, L.; Viswanatha, R.; Klimov, V. I.; Brovelli, S. Large-Area Luminescent Solar Concentrators Based on Stokes-Shift-Engineered Nanocrystals in a Mass-Polymerized PMMA Matrix. *Nat. Photonics* **2014**, *8*, 392−399.
(50) Donega, C. d. M. Synthesis and Properties of Colloidal Heteronanocrystals. *Chem. Soc. Rev.* **2011**, *40*, 1512−1546.
(51) Hadar, I.; Philbin, J. P.; Panfil, Y. E.; Neyshtadt, S.; Lieberman, I.; Eshet, H.; Lazar, S.; Rabani, E.; Banin, U. Semiconductor Seeded Nanorods with Graded Composition Exhibiting High Quantum-Yield, High Polarization, and Minimal Blinking. *Nano Lett.* **2017**, *17*, 2524−2531.
(52) Wang, Q.; Zhang, X.; Jin, Z.; Zhang, J.; Gao, Z.; Li, Y.; Liu, S. F. Energy-Down-Shift $CsPbCl_3$:Mn Quantum Dots for Boosting the Efficiency and Stability of Perovskite Solar Cells. *ACS Energy Lett.* **2017**, *2*, 1479−1486.
(53) Weber, W. H.; Lambe, J. Luminescent Greenhouse Collector for Solar Radiation. *Appl. Opt.* **1976**, *15*, 2299−2300.
(54) Goetzberger, A.; Greube, W. Solar Energy Conversion with Fluorescent Collectors. *Appl. Phys.* **1977**, *14*, 123−139.
(55) Debije, M. G.; Verbunt, P. P. C. Solar Concentrators: Thirty Years of Luminescent Solar Concentrator Research: Solar Energy for the Built Environment. *Adv. Energy Mater.* **2012**, *2*, 12−35.
(56) Meinardi, F.; Ehrenberg, S.; Dhamo, L.; Carulli, F.; Mauri, M.; Bruni, F.; Simonutti, R.; Kortshagen, U.; Brovelli, S. Highly Efficient Luminescent Solar Concentrators Based on Earth-Abundant Indirect-Bandgap Silicon Quantum Dots. *Nat. Photonics* **2017**, *11*, 177−185.
(57) Meinardi, F.; McDaniel, H.; Carulli, F.; Colombo, A.; Velizhanin, K. A.; Makarov, N. S.; Simonutti, R.; Klimov, V. I.; Brovelli, S. Highly Efficient Large-Area Colourless Luminescent Solar Concentrators Using Heavy-Metal-Free Colloidal Quantum Dots. *Nat. Nanotechnol.* **2015**, *10*, 878.
(58) van Sark, W. G. J. H. M. Luminescent Solar Concentrators − a Low Cost Photovoltaics Alternative. *Renewable Energy* **2013**, *49*, 207−210.
(59) Hermann, A. M. Luminescent Solar Concentrators - a Review. *Sol. Energy* **1982**, *29*, 323−329.

DOI: 10.1021/acsenergylett.7b00701
ACS Energy Lett. 2017, 2, 2368−2377

(60) Banal, J. L.; Ghiggino, K. P.; Wong, W. W. H. Efficient Light Harvesting of a Luminescent Solar Concentrator Using Excitation Energy Transfer from an Aggregation-Induced Emitter. *Phys. Chem. Chem. Phys.* **2014**, *16*, 25358−25363.
(61) Currie, M. J.; Mapel, J. K.; Heidel, T. D.; Goffri, S.; Baldo, M. A. High-Efficiency Organic Solar Concentrators for Photovoltaics. *Science* **2008**, *321*, 226−228.
(62) Aste, N.; Tagliabue, L. C.; Del Pero, C.; Testa, D.; Fusco, R. Performance Analysis of a Large-Area Luminescent Solar Concentrator Module. *Renewable Energy* **2015**, *76*, 330−337.
(63) Slooff, L. H.; Bende, E. E.; Burgers, A. R.; Budel, T.; Pravettoni, M.; Kenny, R. P.; Dunlop, E. D.; Büchtemann, A. A Luminescent Solar Concentrator with 7.1% Power Conversion Efficiency. *Phys. Status Solidi RRL* **2008**, *2*, 257−259.
(64) Zhao, Y.; Meek, G. A.; Levine, B. G.; Lunt, R. R. Near-Infrared Harvesting Transparent Luminescent Solar Concentrators. *Adv. Opt. Mater.* **2014**, *2*, 606−611.
(65) van Sark, W.; Moraitis, P.; Aalberts, C.; Drent, M.; Grasso, T.; L'Ortije, Y.; Visschers, M.; Westra, M.; Plas, R.; Planje, W. The "Electric Mondrian" as a Luminescent Solar Concentrator Demonstrator Case Study. *Solar RRL* **2017**, *1*, 1600015.
(66) Debije, M. G. Solar Energy Collectors with Tunable Transmission. *Adv. Funct. Mater.* **2010**, *20*, 1498−1502.
(67) Pietryga, J. M.; Park, Y.-S.; Lim, J.; Fidler, A. F.; Bae, W. K.; Brovelli, S.; Klimov, V. I. Spectroscopic and Device Aspects of Nanocrystal Quantum Dots. *Chem. Rev.* **2016**, *116*, 10513−10622.
(68) Krumer, Z.; Pera, S. J.; van Dijk-Moes, R. J. A.; Zhao, Y.; de Brouwer, A. F. P.; Groeneveld, E.; van Sark, W. G. J. H. M.; Schropp, R. E. I.; de Mello Donega, C. Tackling Self-Absorption in Luminescent Solar Concentrators with Type-II Colloidal Quantum Dots. *Sol. Energy Mater. Sol. Cells* **2013**, *111*, 57−65.
(69) Giebink, N. C.; Wiederrecht, G. P.; Wasielewski, M. R. Resonance-Shifting to Circumvent Reabsorption Loss in Luminescent Solar Concentrators. *Nat. Photonics* **2011**, *5*, 694−701.
(70) Connell, R.; Ferry, V. E. Integrating Photonics with Luminescent Solar Concentrators: Optical Transport in the Presence of Photonic Mirrors. *J. Phys. Chem. C* **2016**, *120*, 20991−20997.
(71) Bronstein, N. D.; Yao, Y.; Xu, L.; O'Brien, E.; Powers, A. S.; Ferry, V. E.; Alivisatos, A. P.; Nuzzo, R. G. Quantum Dot Luminescent Concentrator Cavity Exhibiting 30-Fold Concentration. *ACS Photonics* **2015**, *2*, 1576.
(72) Desmet, L.; Ras, A. J. M.; de Boer, D. K. G.; Debije, M. G. Monocrystalline Silicon Photovoltaic Luminescent Solar Concentrator with 4.2% Power Conversion Efficiency. *Opt. Lett.* **2012**, *37*, 3087−3089.
(73) Goldschmidt, J. C.; Peters, M.; Bösch, A.; Helmers, H.; Dimroth, F.; Glunz, S. W.; Willeke, G. Increasing the Efficiency of Fluorescent Concentrator Systems. *Sol. Energy Mater. Sol. Cells* **2009**, *93*, 176−182.
(74) Zhou, Y.; Benetti, D.; Fan, Z.; Zhao, H.; Ma, D.; Govorov, A. O.; Vomiero, A.; Rosei, F. Near Infrared, Highly Efficient Luminescent Solar Concentrators. *Adv. Energy Mater.* **2016**, *6*, 1501913.
(75) Bradshaw, L. R.; Knowles, K. E.; McDowall, S.; Gamelin, D. R. Nanocrystals for Luminescent Solar Concentrators. *Nano Lett.* **2015**, *15*, 1315−1323.
(76) Coropceanu, I.; Bawendi, M. G. Core/Shell Quantum Dot Based Luminescent Solar Concentrators with Reduced Reabsorption and Enhanced Efficiency. *Nano Lett.* **2014**, *14*, 4097−4101.
(77) Bomm, J.; Büchtemann, A.; Fiore, A.; Manna, L.; Nelson, J. H.; Hill, D.; van Sark, W. G. J. H. M. Fabrication and Spectroscopic Studies on Highly Luminescent CdSe/CdS Nanorod Polymer Composites. *Beilstein J. Nanotechnol.* **2010**, *1*, 94−100.
(78) Li, H.; Wu, K.; Lim, J.; Song, H.-J.; Klimov, V. I. Doctor-Blade Deposition of Quantum Dots onto Standard Window Glass for Low-Loss Large-Area Luminescent Solar Concentrators. *Nat. Energy* **2016**, *1*, 16157.
(79) Erickson, C. S.; Bradshaw, L. R.; McDowall, S.; Gilbertson, J. D.; Gamelin, D. R.; Patrick, D. L. Zero-Reabsorption Doped-Nanocrystal Luminescent Solar Concentrators. *ACS Nano* **2014**, *8*, 3461−3467.
(80) Knowles, K. E.; Kilburn, T. B.; Alzate, D. G.; McDowall, S.; Gamelin, D. R. Bright $CuInS_2$/CdS Nanocrystal Phosphors for High-Gain Full-Spectrum Luminescent Solar Concentrators. *Chem. Commun.* **2015**, *51*, 9129−9132.
(81) Hu, X.; Kang, R.; Zhang, Y.; Deng, L.; Zhong, H.; Zou, B.; Shi, L.-J. Ray-Trace Simulation of $CuInS(Se)_2$ Quantum Dot Based Luminescent Solar Concentrators. *Opt. Express* **2015**, *23*, A858−A867.
(82) Chen, W.; Li, J.; Liu, P.; Liu, H.; Xia, J.; Li, S.; Wang, D.; Wu, D.; Lu, W.; Sun, X. W. Heavy Metal Free Nanocrystals with near Infrared Emission Applying in Luminescent Solar Concentrator. *Solar RRL* **2017**, *1*, 1700041.
(83) Klimov, V. I.; Baker, T. A.; Lim, J.; Velizhanin, K. A.; McDaniel, H. Quality Factor of Luminescent Solar Concentrators and Practical Concentration Limits Attainable with Semiconductor Quantum Dots. *ACS Photonics* **2016**, *3*, 1138−1148.
(84) Zhao, H.; Zhou, Y.; Benetti, D.; Ma, D.; Rosei, F. Perovskite Quantum Dots Integrated in Large-Area Luminescent Solar Concentrators. *Nano Energy* **2017**, *37*, 214−223.
(85) Lin, C. C.; Xu, K. Y.; Wang, D.; Meijerink, A. Luminescent Manganese-Doped $CsPbCl_3$ Perovskite Quantum Dots. *Sci. Rep.* **2017**, *7*, 45906.
(86) Beaulac, R.; Archer, P. I.; Ochsenbein, S. T.; Gamelin, D. R. Mn^{2+}-Doped CdSe Quantum Dots: New Inorganic Materials for Spin-Electronics and Spin-Photonics. *Adv. Funct. Mater.* **2008**, *18*, 3873−3891.
(87) O'Leary, K.; Paul, D. R. Copolymers of Poly(N-Alkyl Acrylates): Synthesis, Characterization, and Monomer Reactivity Ratios. *Polymer* **2004**, *45*, 6575−6585.
(88) Beiner, M.; Schroter, K.; Hempel, E.; Reissig, S.; Donth, E. Multiple Glass Transition and Nanophase Separation in Poly(N-Alkyl Methacrylate) Homopolymers. *Macromolecules* **1999**, *32*, 6278−6282.
(89) Puig, J.; Williams, R. J. J.; Hoppe, C. E. Poly(Dodecyl Methacrylate) as Solvent of Paraffins for Phase Change Materials and Thermally Reversible Light Scattering Films. *ACS Appl. Mater. Interfaces* **2013**, *5*, 9180−9185.
(90) Jellicoe, T. C.; Richter, J. M.; Glass, H. F. J.; Tabachnyk, M.; Brady, R.; Dutton, S. E.; Rao, A.; Friend, R. H.; Credgington, D.; Greenham, N. C.; et al. Synthesis and Optical Properties of Lead-Free Cesium Tin Halide Perovskite Nanocrystals. *J. Am. Chem. Soc.* **2016**, *138*, 2941−2944.
(91) Yang, B.; Chen, J.; Hong, F.; Mao, X.; Zheng, K.; Yang, S.; Li, Y.; Pullerits, T.; Deng, W.; Han, K. Lead-Free, All-Inorganic Cesium Bismuth Halide Perovskite Nanocrystals with Long-Term Stability. *Angew. Chem., Int. Ed.* **2017**, DOI: 10.1002/anie.201704739.

DOI: 10.1021/acsenergylett.7b00701
ACS Energy Lett. 2017, 2, 2368−2377